Appl. Math. Mech. -Engl. Ed., **42**(2), 159–172 (2021)

APPLIED MATHEMATICS AND MECHANICS (ENGLISH EDITION)

https://doi.org/10.1007/s10483-021-2705-7

Soft pneumatic actuators by digital light processing combined with injection-assisted post-curing*

Qiang ZHANG[1], Shayuan WENG[2], Zeang ZHAO[3], H. J. QI[4], Daining FANG[1,3,†]

1. State Key Laboratory for Turbulence and Complex System, College of Engineering, Peking University, Beijing 100871, China;
2. College of Aerospace Engineering, Chongqing University, Chongqing 400044, China;
3. Institute of Advanced Structure Technology, Beijing Institute of Technology, Beijing 100081, China;
4. The George W. Woodruff School of Mechanical Engineering, Georgia Institute of Technology, Atlanta, GA 30332, U. S. A.

(Received Nov. 26, 2020 / Revised Dec. 2, 2020)

Abstract The soft robotics display huge advantages over their rigid counterparts when interacting with living organisms and fragile objects. As one of the most efficient actuators toward soft robotics, the soft pneumatic actuator (SPA) can produce large, complex responses with utilizing pressure as the only input source. In this work, a new approach that combines digital light processing (DLP) and injection-assisted post-curing is proposed to create SPAs that can realize different functionalities. To enable this, we develop a new class of photo-cross linked elastomers with tunable mechanical properties, good stretchability, and rapid curing speed. By carefully designing the geometry of the cavities embedded in the actuators, the resulting actuators can realize contracting, expanding, flapping, and twisting motions. In addition, we successfully fabricate a soft self-sensing bending actuator by injecting conductive liquids into the three-dimensional (3D) printed actuator, demonstrating that the present method has the potential to be used to manufacture intelligent soft robotic systems.

Key words soft pneumatic actuator (SPA), digital light processing (DLP), injection-assisted post-curing, three-dimensional (3D) printing

Chinese Library Classification O343
2010 Mathematics Subject Classification 11C08, 74S05, 74B05

1 Introduction

Over the last decade, the soft robotics have gained more and more research interest because of its prominent advantages over rigid robotics in terms of continuous deformation ability, in-

* Citation: ZHANG, Q., WENG, S. Y., ZHAO, Z. A., QI, H. J., and FANG, D. N. Soft pneumatic actuators by digital light processing combined with injection-assisted post-curing. *Applied Mathematics and Mechanics* (*English Edition*), **42**(2), 159–172 (2021) https://doi.org/10.1007/s10483-021-2705-7

† Corresponding author, E-mail: fangdn@pku.edu.cn

Project supported by the National Natural Science Foundation of China (Nos. 11572002 and 12002032) and the China Postdoctoral Science Foundation (Nos. BX20200056 and 2020M670149)

creased flexibility and adaptability for accomplishing tasks, and improved safety[1–6]. These characteristics allow for its potential applications in the fields of food sorting[7–8] and disaster relief scenarios[9–10]. Till now, various control methods and materials have been exploited to act as the actuation system for soft robotics, to allow for movement and interaction with the surrounding environment. For example, electrostatic force such as high-voltage electric field can be utilized to drive dielectric elastomer actuators (DEAs) to change shape and respond, producing high forces, large strains, as well as high energy density[11–12]. However, high electric fields make DEAs prone to failure from dielectric breakdown and electrical aging[13]. As another example, shape memory polymers (SMPs), especially two-way SMPs that can produce reversible shape change without manual intervention, can be used for actuation[14–15]. But some drawbacks exist for SMPs such as low response (> 10 s) and typically low force generated[16–17].

The pneumatic loading has recently been exploited to actuate various soft pneumatic actuators (SPAs) with overcoming the disadvantages that exist in the above methods[18–23]. Utilizing pressure as the only input source, SPAs can produce a rapid response and a large force, allowing for various motions including bending, twisting, grabbing, and contracting[24–26], and thus have significantly promoted the development of the field of soft robotics. However, the fabrication of most of the current SPAs still relies on casting, assembling, and gluing, which could cause delamination between glued parts and lead to failure[18]. Very recently, three-dimensional (3D) printing has been utilized to manufacture SPAs by printing a wide range of silicone inks[27–29]. Schaffner et al.[30] reported a direct-ink writing (DIW) based 3D printing platform for the seamless digital fabrication of pneumatic silicone actuators exhibiting programmable bioinspired architectures and motions. Although promising, when printing cylindrical actuators, they can hardly print soft cylindrical parts without the help from a rotating support. A similar dilemma was met when Truby et al.[31] utilized DIW to print somatosensitive actuators. In their work, three mold layers are adopted to define the shape of the actuator as well as to provide support. Due to the printing characteristics of DIW, it is essentially very challenging to directly print free-standing structures from uncured materials with extremely low shear modulus. By contrast, digital light processing (DLP) 3D printing works by selectively curing a layer of photocurable resin at a time via UV light and then repeats the process in a layer-by-layer manner, allowing to print soft materials without the assistance of support. This was first demonstrated by Patel et al.[32] in 2017 by using heated-assisted DLP to print pneumatic grippers. Later, their group advanced the printing of SPAs by fabricating soft pneumatic robots on millimeter scales with microscale voids and channels[33–34]. However, their approach requires a DLP instrument equipped with special functionalities (e.g., heating or air jet cleaning), which may decrease the manufacturing speed and increase the operational difficulties. In principle, 3D printing is capable of printing structures in arbitrary shapes; therefore, it is very desired to advance 3D printing of SPAs in a more feasible, simple, and accessible way.

Here, we propose a new approach to fabricate soft pneumatic actuators based on the combination of DLP injection-assisted post-curing. To do this, room temperature-DLP is firstly used to print a series of actuator 'green' parts with pre-designed microscale cavities. Then, functional liquids are injected into the cavities, and photocurable resin droplets are used to encapsulate the cavity inlets and outlets. The obtained sample is subsequently transferred into a UV box for post-curing. Depending on the requirements, the functional liquid can be a photocurable resin with a high cured modulus to provide a distinct mechanical property from the bulk material of the actuator, or a conductive liquid such as liquid metal or ionic solution to provide sensing functionalities. To realize our method, a new material system with good stretchability as well as tunable mechanical properties is developed. Based on varied designs, the SPAs we create can realize responses including contracting, expanding, flapping, twisting, and self-sensing while bending. We believe the approach proposed here will accelerate the manufacturing of complex and functional SPAs.

2 Materials and methods

2.1 Preparation of materials

The liquid resin used for printing SPAs in this work is prepared by first mixing three monomers consisting of 2-hydroxyethyl acrylate (HEA), butyl acrylate (BA), and isodecyl acrylate (IA) at a weight ratio of 4.62:1.92:1. Then we mix the above mixtures with crosslinker aliphatic urethane diacrylate (AUD, EBECRYL® 8807), photoinitiator phenylbis (2, 4, 6-trimethylbenzoyl) phosphine oxide, and photo absorber Sudan I at a weight ratio of 64.26:35:0.7:0.04 to obtain resin M-35, a weight ratio of 89.26:10:0.7:0.04 to obtain resin M-10, and a weight ratio of 97.26:2:0.7:0.04 to obtain resin M-2, respectively. 'M' represents 'material' and '35' or '10' or '2' represents the percentage of crosslinker. The photoinitiator is used to trigger photopolymerization reaction while the photo absorber is used to limit the UV light scattering during printing. The AUD is donated from Allnex (Alpharetta, GA, U. S. A.), and the rest of the chemicals are all purchased from Sigma-Aldrich (St. Louis, MO, U. S. A.). All the reagents are used as received without any modification.

2.2 DLP and injection-assisted post-curing

The DLP instrument used in this work is composed of a UV light projector with a built-in DMD (Texas Instruments, Dallas, Texas, U. S. A.), and a linear motion stage (LTS150, Thorlabs, Newton, NJ, U. S. A.). A MATLAB (The MathWorks, Inc., Natick, MA, U. S. A.) script is written to coordinate the projecting operation and moving operation to enable the layer-by-layer printing. Before printing, a radiometer (IL1400A, International Light Technologies, Peabody, MA, U. S. A.) is used to measure the light intensity of the UV light emitted from the projector. The light intensity used for printing is set as 11.4 $\mathrm{m{\cdot}W{\cdot}cm^{-2}}$. The layer thickness and printing time for each layer are set as 100 μm and 2 s, respectively. After printing, a 5 cc syringe is used to inject functional liquids into the reserved microscale cavities in the sample. The entire sample is then transferred to a UV box for post-curing.

2.3 Rheology characterization and mechanical tests

A ThermoHaake RS300 rheometer (Thermo Fisher Scientific, Waltham, MA, U. S. A.) with a cone-plate sensor is utilized to characterize the viscosity of the three resins. The sensor is equipped with a diameter of 35 mm, a cone angle of 2°, and a gap of 1 mm. All measurements are carried out under ambient conditions. The stress-strain curve of each tensile specimen (about 25 mm × 4.5 mm × 0.1 mm) is measured using a DMA tester (model Q800, TA Instruments) in a strain mode at a constant rate of 6 mm/min. For each material, at least five specimens are tested.

2.4 Data collecting of actuators and sensors

To realize actuating, we first connect the actuator with a high-precision pressure controller, Ultimus V pressure regulator (Nordson Corporation, Westlake, OH, U. S. A.), through a dispensing tip and tubes (with an inner diameter of about 3 mm), and then apply air pressure according to a preset value. During actuating, we use a digital camera, Canon EOS 50D (Canon Inc., Ota, Tokyo, Japan), to record the deforming process of the actuator. The resistance change of the sensing element is collected by a digit multimeter (Keithley 2100, Keithley Instruments, Solon, OH, U. S. A.), which sends data to a computer for real-time display through MATLAB communication code.

2.5 Analytic modeling and finite element analysis (FEA)

The analytic model used for predicting the behavior of the twisting actuators under different conditions is established based on the assumption that the stiff fibers and soft matrix can be simplified as a fiber-reinforced cylindrical shell. We only model the linear, small-displacement deformation to show the effects of the design parameters on the mechanical responses of the actuator. Details of the derivation can be found in Appendix A. We also conduct the FEA to model the nonlinear deformation of the butterfly-like actuator using software package ABAQUS (v6.13, Simulia, Providence, RI, U. S. A.). To guarantee the consistency between FEA and ex-

periments, the geometric model used for FEA is the same as that used for printing. In the simulation, ten-node 3D incompressible solid elements (C3D10H) with refined meshes are attached to the numerical model. The geometry is virtually inflated by applying uniform pressure inside the surface of cavities. The end of the actuator is fixed to guarantee a fully clamped boundary condition as used in experiments. A double-parameter Mooney-Rivlin constitutive model is employed to describe the mechanical behavior of the actuator materials. The material parameters in the model are determined through uniaxial tensile tests and more details can be found in Appendix B.

3 Results and discussion

3.1 DLP 3D printing and material system

The 3D printing procedure for SPAs is depicted in Fig. 1(a). In the first step, a DLP 3D printer is used to print highly stretchable materials into structures with reserved cavities. In the second step, functional liquids are injected into the cavities through a syringe. The obtained sample is then transferred to a UV box for post-curing. To enable 3D printing of SPAs in high resolution as well as high deformability, we set out to formulate a photocurable resin that would have: (i) an extremely low viscosity with excellent fluidity to allow room-temperature printing, (ii) a rapid curing speed to allow fast printing, and (iii) relatively low glass transition temperature to enable the resulting materials with good stretchability. Here, we formulate the resin by mixing three commercially available vinyl monomers, HEA, BA, and IA, at a weight ratio of 4.62:1.92:1. To allow the mechanical properties of the materials to be tunable, we mix the above monomers with a varied amount of the AUD, and obtain three photosensitive resins, namely, M-35, M-10, and M-2. Figure 1(b) shows the chemical structure of the three monomers. With the formulated liquid resin, various soft structures can be printed and post-cured. In Fig. 1(c), we present an octet-based lattice structure printed using resin M-10. It is observed that the lattice is in excellent good shape and can be deformed easily.

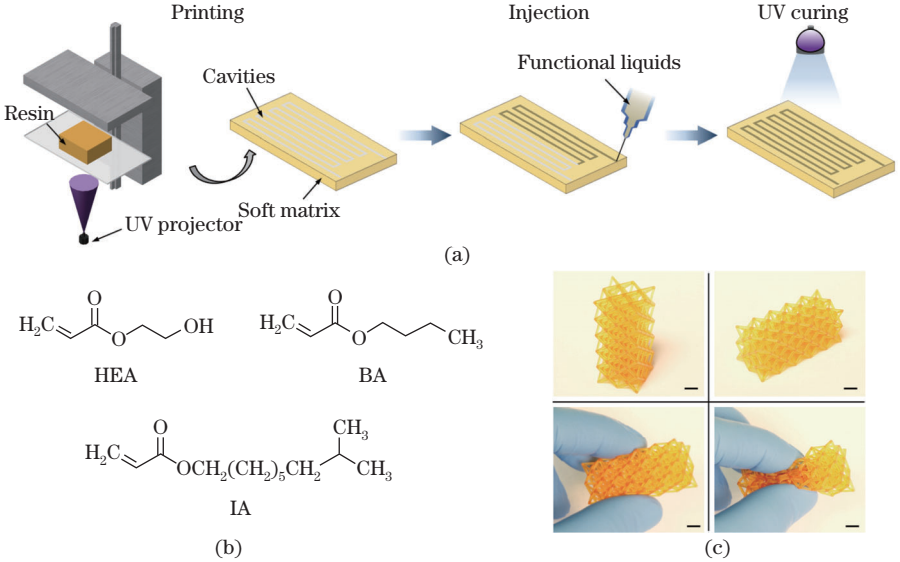

Fig. 1 (a) Schematic illustration of 3D printing and injection-assisted post-curing. (b) Chemical structures of the monomers used in the material systems. (c) 3D printed octet-based lattice showing the high-resolution printing ability and the deformation ability of the structure (all scale bars are 5 mm) (color online)

3.2 Characterizations of resins and photo-crosslinked materials

Before we start to print SPAs, we first characterize the properties of the obtained three resins and the mechanical properties of the materials cured from the resins. In Fig. 2(a), we present the apparent viscosity versus shear rate for the three resins. It is observed that with increasing the amount of the crosslinker from 2% to 35%, the viscosity of the resin increases from $0.002\,\mathrm{Pa}\cdot\mathrm{s}$ to $0.065\,\mathrm{Pa}\cdot\mathrm{s}$; for resin M-2, the viscosity is very low and is comparable with water (at room temperature). It should be noted that all the resins fabricated here can be directly printed into intricate geometries at room temperature without the necessity of heating[35]. To investigate the curing speed of the three kinds of resins, we pipette resin droplets onto a piece of a glass slide and use another piece of glass slide to cover the droplets; the gap between the two slides is determined by the spacers (about 0.7 mm). We then project UV light (with the light intensity fixed at 7.16 $\mathrm{m\cdot W\cdot cm^{-2}}$) from one side and measure the thickness (or curing depth) of the cured sample sheet for different irradiation times. As shown in Fig. 2(b), for the same irradiation time, the more the crosslinker content is, the larger the curing depth can be, which indicates that we can increase the curing speed by adding more crosslinkers; we also notice that for resin M-2, the fast curing speed allows us to obtain a relatively thick sheet (180 μm) within only two seconds, which permits a rapid printing. The materials used for soft pneumatic actuators need to be elastomeric and stretchable. We investigate the mechanical properties of the materials (namely, M-35, M-10, and M-2) cured from the three resins using uniaxial tensile tests. Figure 2(c) shows the stress-strain curves of the three materials obtained from the tests.

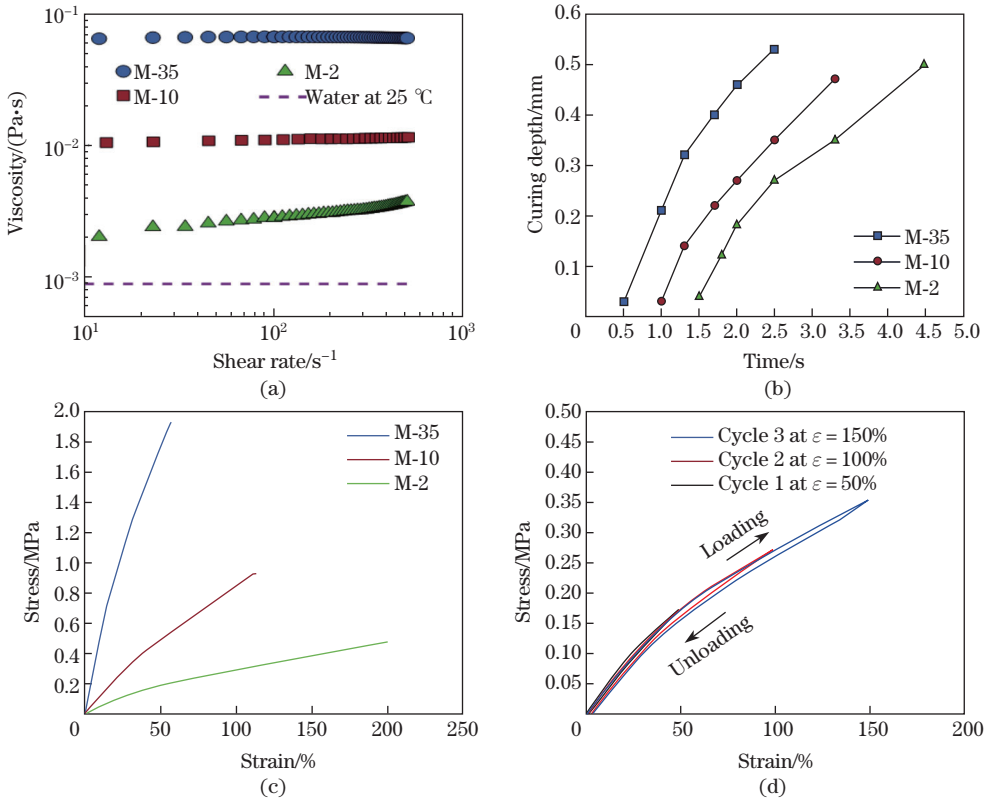

Fig. 2 (a) Viscosity as a function of shear rate for resin M-35, resin M-10, resin M-2, and water at 25 °C. (b) Curing depth as a function of irradiation time for resin M-35, M-10, and M-2. (c) Uniaxial stress-strain curves for materials M-35, M-10, and M-2. (d) Stress-strain curves for material M-2 under three loading/unloading cycles at a maximum strain of 50%, 100%, and 150%, respectively (color online)

It is observed that as the content of the crosslinker increases from 2% to 35%, Young's modulus of the material increases from 531 kPa to 4.72 MPa while the elongation at break decreases from 200% to 65%; for material M-2, its elongation at break is comparable to the most stretchable commercially UV-curable material (i.e., Tangoplus FLX930, with an elongation at break of 170%–220%)[33]. To further study the cyclic mechanical properties of our material systems, we use M-2 as the representative object and stretch the material to strain $\varepsilon = 50\%$, $\varepsilon = 100\%$, and $\varepsilon = 150\%$ followed by unloading in each cycle. It is observed that during each cycle, the loading and unloading curves nearly coincide with each other and shows no prominent hysteresis; moreover, the loading curve in the current cycle overlaps with the loading curve in the previous cycle. These results demonstrate that our material systems exihibit nearly pure elastomeric behavior with negligible dissipation mechanisms (e.g., viscoelastic and Mullin's effect), demonstrating advantages over other material systems in terms of generating repeatable mechanical responses for soft actuators[32].

3.3 3D printing SPAs

Inspired by the flexible structure of an accordion, we use resin M-2 to print an accordion-based actuator that can contract/elongate along the actuator axis upon applying negative/positive pressure. Due to its ability to elongate or contract along the axial direction, the actuator can be exploited to lift a weight up or put the weight down by controlling pressure. For example, the actuator can lift 20 g weight to 4.1 mm high when a negative pressure of 4.61 kPa is applied (right in Fig. 3(a)) and then release the weight down when the pressure recovers to zero. This process can be repeated many times. Figure 3(b) presents an actuator (printed using resin M-2) in a hollow cubic shape. Upon applying positive pressure, it can expand into a larger configuration tending to be spherical. When the pressure achieves 44.8 kPa, the horizontal stretch becomes 3, showing a remarkably large deformation. This large-deformation capability of the actuator can be used for sensing if there are obstacles around. We demonstrate this by connecting the actuator to a syringe that can apply a vertical displacement load. Firstly, we record the load-displacement curve during the expanding process when there are no obstacles around as the reference (blue curve in Fig. 3(b)). Next, during a new expanding process, we sometimes move obstacles toward the actuator and sometimes move the obstacles away from the actuator. Since when there are obstacles around the actuator, the measured load (red curve in Fig. 3(b)) will be higher than that of the reference state (due to increased stiffness from the restriction), and when the obstacles are removed, the measured load will overlap with the reference, we can easily judge when there are obstacles and when there are no obstacles based on the difference between the two curves. Except for the above two examples with relatively large cavities, we next present an actuator consisting of intricate cavities with the cross-section in micro scales. As illustrated in Fig. 3(c) (left), the wings of a butterfly in nature are composed of membranes with skeletons in complex geometry. Here, we are interested in mimicking the structure of the wings and their flapping motions. To do this, we design an actuator that shares the same contour with the butterfly wings; inside the actuator, we draw the micro-cavities following the trajectory of the skeletons in the real wings (Fig. 3(c), middle). For a rectangular building block with an embedded cavity inside, upon applying pressure, the block tends to bend toward the side where the stiffness is higher. Based on this mechanism, the printed actuator (using resin M-2) shown in Fig. 3(c) (right) will bend inward upon applying pressure, mimicking the flapping motions of butterfly wings. We test the motion of the printed actuator by applying periodic pressure signals with different frequencies (0.5 Hz, 2 Hz, and 10 Hz) as well as peak values (54 kPa, 86 kPa, and 108 kPa). The top panel of Fig. 3(d) shows the flapping-downward motion process in which the pressure is increasing, while the bottom panel of Fig. 3(d) shows the flapping-upward motion process in which the pressure is decreasing. It is observed that the actuator responds rapidly according to the applied pressure. We further conduct the FEA on the deformation of the actuator when pressurized. Figure 3(e) (top panel) shows the comparison results on the deformed configuration between the experiment and

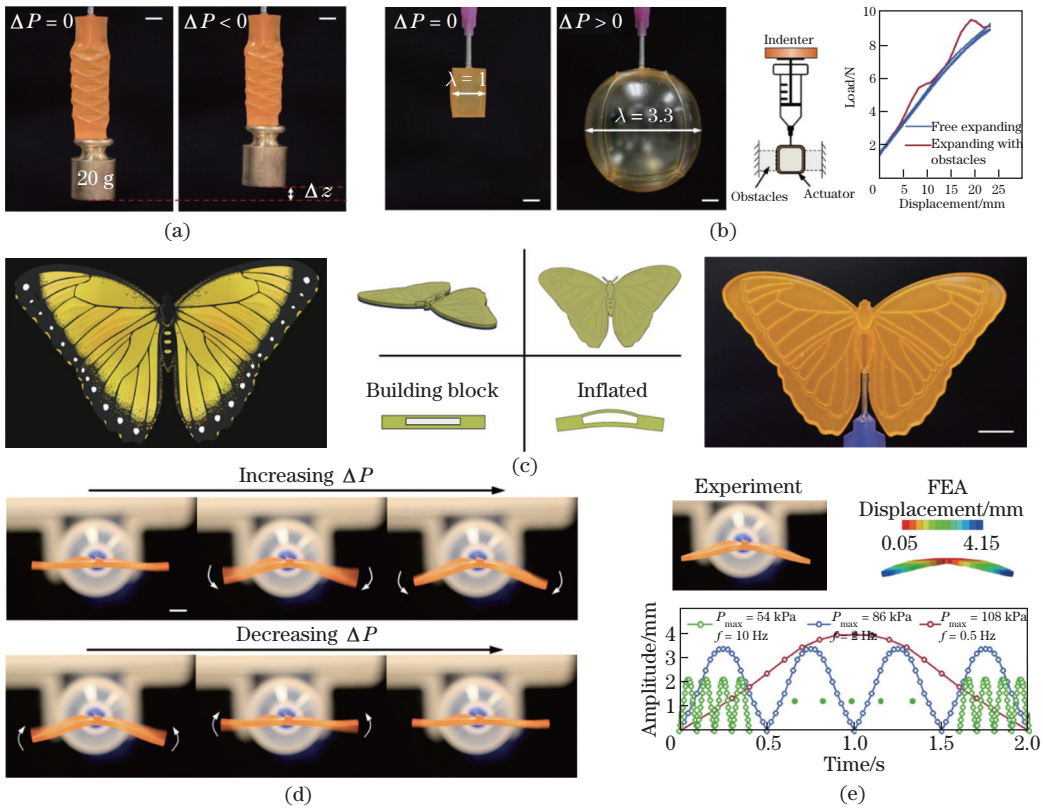

Fig. 3 (a) Accordion based actuator contracting and lifting 20 g weight upon applying negative pressure. Δz is about 4.1 mm when ΔP is -4.61 kPa. (b) Cube-like actuator expanding into a spherical shape upon applying positive pressure (left). The horizontal stretch becomes 3 when the pressure achieves 44.8 kPa. Measured load-displacement curves during the expanding process with the absence (blue) and presence (red) of obstacles. (c) Butterfly-like actuator mimicking the geometry as well as the flapping motion of butterfly wings. From left to right, butterfly in nature, design, and printed butterfly-like actuator. (d) Snapshots of the flapping process of the butterfly-like actuator. (e) FEA of the deformation of the butterfly-like actuator. The top panel shows the vertical displacement distribution inside the actuator when the pressure reaches 108 kPa, while the bottom panel shows the amplitude (vertical displacement of the tip of the wings) as a function of time for three different pressure inputs (all scale bars are 5 mm) (color online)

FEA when the pressure reaches 108 kPa. Figure 3(e) (bottom panel) also presents the results on the amplitude-time curves obtained from three different pressure input signals. It can be seen that the amplitude periodically changes with time and is closely related to the pressure input.

3.4 Twisting actuators by 3D printing and injection-assisted post-curing

The high-resolution DLP printing as well as the material systems proposed here allows us to realize richer functions in the resulting actuators by combining 3D printing with injection-assisted post-curing. Here, we present actuators that can twist upon applying pressure by first 3D printing cylindrical tubes with helical cavities in the shell and then injecting liquid photosensitive resin (poly (ethylene glycol) diacrylate, average Mn 250 (PEGDA 250)) into those cavities and allowing them to be cured together in the post-curing process. The PEGDA 250 is chosen here to provide a high modulus (about 700 MPa) for restricting the undesired expansion of the tube upon applying pressure. As illustrated in Fig. 4(a), the twisting actuator

consists of four stiff fibers (made of PEGDA 250) and a soft matrix (made of M-2). To enable the twisting deformation of the actuator upon expanding, we arrange the fibers in a helical orientation wherein the lead angle can be changed. Here, we choose three lead angle values ($\alpha_1 = 83.8°$, $\alpha_2 = 77.8°$, and $\alpha_3 = 66.6°$) as examples and create three twisting actuators accordingly. Then we study the performance of the actuators by ramping up the pressure and recording the shape-changing. In Fig. 4(b), we present a series of the configuration of the actuator ($\alpha_3 = 66.6°$) at varied pressure values (from 0 psi to 19 psi (1 psi=6.895 kPa)). It is observed that the actuator twists around its axis upon applying pressure and as the pressure increases, the angle increases and achieves 120° when the pressure reaches 19 psi, showing good controllability. In Fig. 4(c), we show the measured twisting angle as a function of pressure for all the three printed actuators. We notice that for the same applied pressure, with a lower lead angle, a larger twisting angle can be achieved, demonstrating that the lead angle is a good design parameter for tunning the mechanical responses of the twisting actuator. The results obtained from the small-displacement theoretical model are also plotted in Fig. 4(c) and show good agreement with experiments for the pressure range lower than 12 psi. To guide the design of the twisting actuators, based on the small-displacement theoretical model, we present the heat map of the twisting angle with the design space constructed by the lead angle and the pressure, as illustrated in Fig. 4(d). Based on the heat map, it is very intuitive to select the design point that corresponds to the desired twisting response.

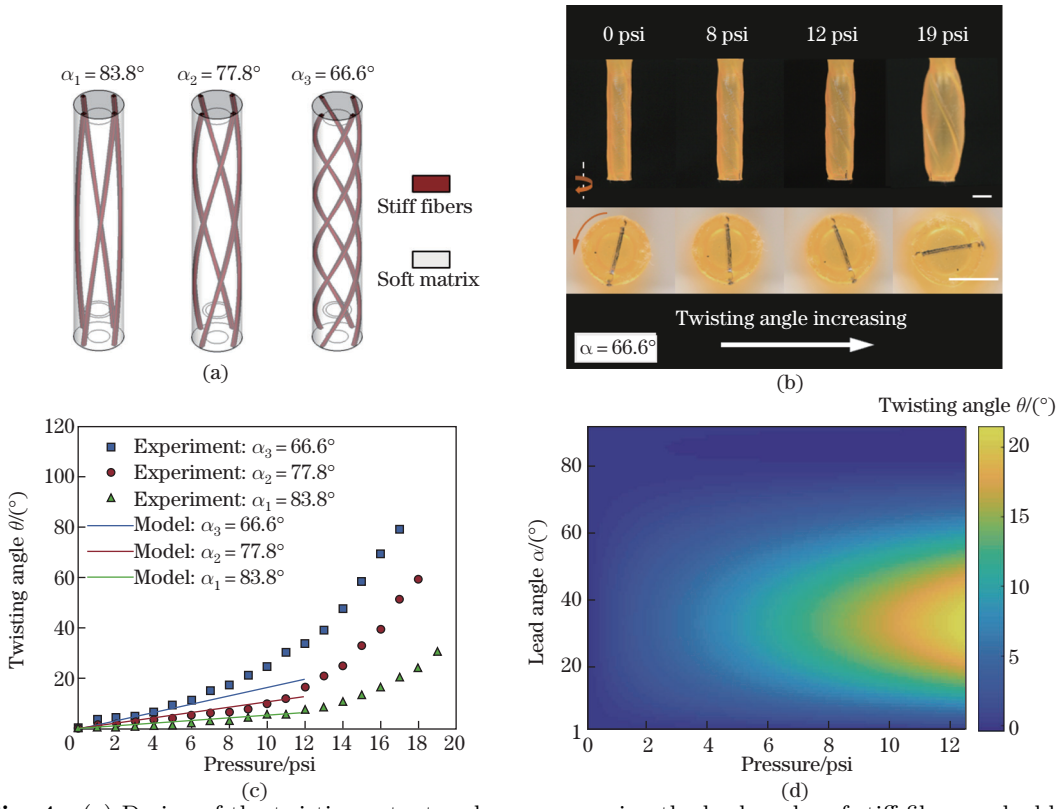

Fig. 4 (a) Design of the twisting actuators by programming the lead angles of stiff fibers embedded in the soft matrix. (b) Snapshots of the twisting deformation process of a twisting actuator with the lead angle set to be 66.6°. Top panel, front view; bottom panel, bottom view (scale bar is 5 mm). (c) Predicted (solid lines) and measured (dots) twisting angle as a function of pressure for actuators with three different lead angles. (d) Heat map showing the twisting angle as a function of lead angle (from 1° to 89°) and pressure (from 0 psi to 12 psi) (color online)

3.5 Soft self-sensing bending actuator by 3D printing and injection-assisted post-curing

By injecting conductive liquids such as liquid metals[36–37] into the reserved microscale cavities, we can endow sensing functionalities into the SPAs to obtain self-sensing actuators. To do this, we first begin with fabricating soft strain sensors that can sustain relatively large deformation. In Fig. 5(a), we present a soft strain sensor with the sensing element designed in a straight line. The material used for this sensor is M-10. It is observed that the sensor can be

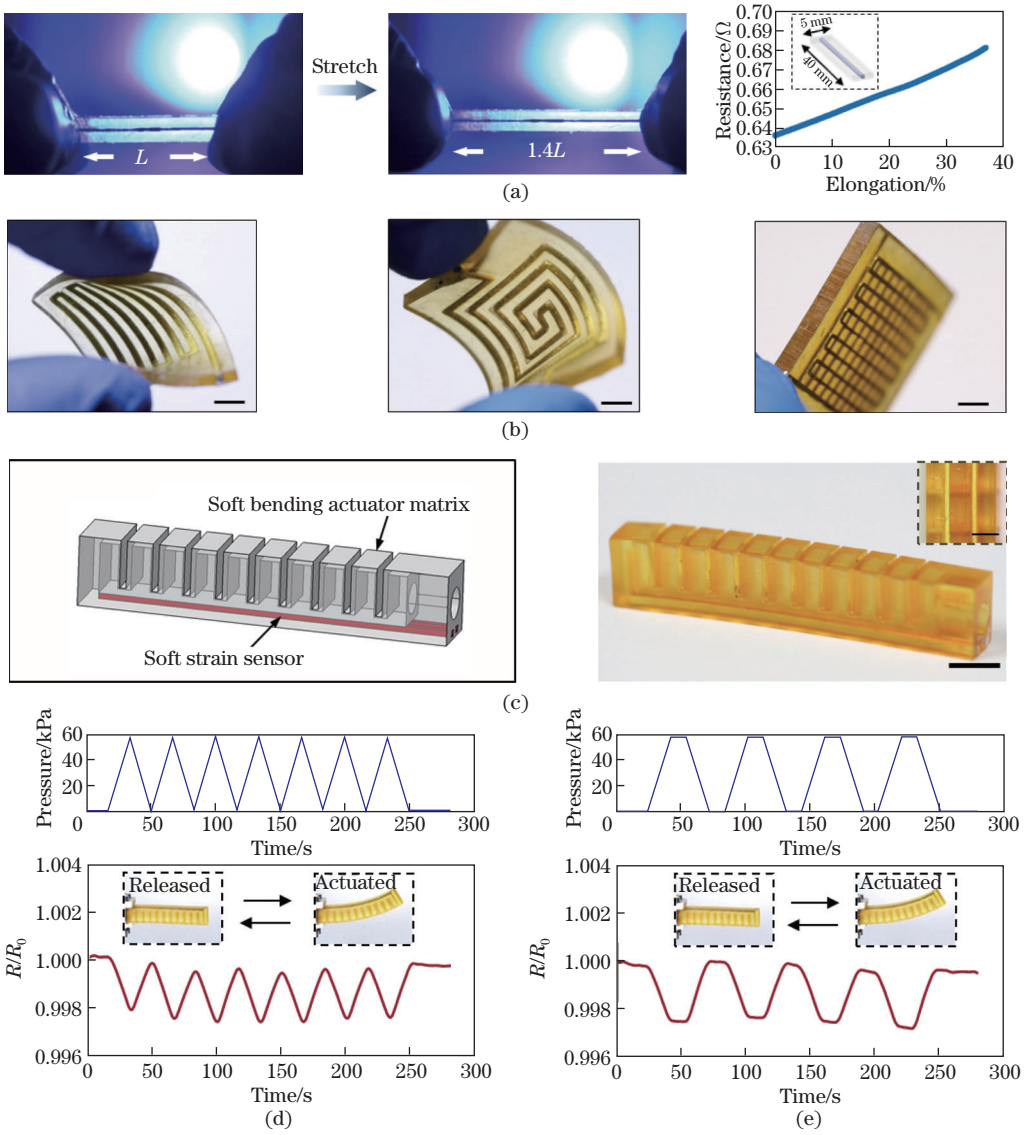

Fig. 5 (a) Soft strain sensor with the sensing element designed in a straight line. When uniaxially stretching the sensor from 0 to 40% strain, the resistance changes accordingly from 0.637 Ω to 0.682 Ω. (b) Soft strain sensors with the sensing meander lines designed in 'U' shape (left), square shape (middle), and dual-layer 'U' shape (right). (c) Schematic illustration of a soft self-sensing bending actuator (left) and the printed actuator (right). (d) Sensing output of the self-sensing actuator when the pressure input is programmed in a triangular waveform. (e) Sensing output of the self-sensing actuator when the pressure input programmed is in a trapezoidal waveform (all scale bars are 5 mm) (color online)

easily stretched to 40% strain; during the stretching process, the resistance of the sensor keeps increasing from 0.637 Ω to 0.682 Ω. Thanks to the printing flexibility by DLP, the shape of the sensing element can be easily changed. For example, the shape of the sensing meander lines can be designed to be in a 'U' shape or a square shape, or even in a dual-layer 'U' shape, as shown in Fig. 5(b). To demonstrate the capability of our method to fabricate self-sensing actuators, here, we present a soft self-sensing bending actuator, as shown in Fig. 5(c). With this design, the actuator bends upon applying pressure; at the same time, the back of the actuator deforms and causes the resistance of the soft sensor to change. Figure 5(c) also presents the experimentally fabricated self-sensing actuator, in which the shape, as well as the sensing element, has high resolution and quality. To evaluate the performance of the actuator, we measure the sensing output of the actuator at the pressure input with different waveforms. In Fig. 5(d), when the pressure input is programmed in a triangular waveform (the top panel), the actuator periodically performs bending and recovering (to the initially undeformed state) motions. During this process, it is observed that the built-in sensor can accurately capture the bending state of the actuator and also outputs a triangular waveform resistance change signal (the bottom panel). Moreover, consistent with the actuating process, the sensing output is in real time. To further test the performance of the self-sensing actuator, we next program the pressure input in a trapezoidal waveform, as shown in Fig. 5(e) (top panel). With this form, the pressure keeps unchanged for a while (12 s) when it reaches the peak or zero, and accordingly, the deformed state or the initially undeformed state of the actuator holds for a while during the actuating process. We are interested in whether the sensor embedded in the actuator can identify this. In Fig. 5(e) (bottom panel), we present the results of the sensing output. It is shown that the resistance change signal does exhibit a trapezoidal waveform; when the pressure is maintained, the signal keeps unchanged, and once the pressure changes, the signal responds immediately and reflects the change of the pressure.

4 Conclusions

In this work, we combine the high-resolution of DLP printing and flexibility of injection-assisted post-curing to provide a new approach for fabricating SPAs that can realize different motions or functionalities. A new photocurable material system enabling rapid curing, good stretchability, and tunable mechanical properties is developed for room temperature-DLP printing with high resolution. By varying the geometry of the cavities and the actuator, we can realize motions including contracting, expanding, and flapping. By injecting conductive liquids, we fabricate a soft self-sensing actuator that can sense the bending deformation while actuating, thus providing the potential possibilities for soft intelligent robotic systems. We believe the approach proposed here will accelerate the manufacturing of complex and functional SPAs.

References

[1] TRIVEDI, D., RAHN, C. D., KIER, W. M., and WALKER, I. D. Soft robotics: biological inspiration, state of the art, and future research. *Applied Bionics and Biomechanics*, **5**(3), 99–117 (2008)

[2] RUS, D. and TOLLEY, M. T. Design, fabrication and control of soft robots. *nature*, **521**(7553), 467–475 (2015)

[3] LASCHI, C., MAZZOLAI, B., and CIANCHETTI, M. Soft robotics: technologies and systems pushing the boundaries of robot abilities. *Science Robotics*, **1**(1), eaah3690 (2016)

[4] HINES, L., PETERSEN, K., LUM, G. Z., and SITTI, M. Soft actuators for small-scale robotics. *Advanced Materials*, **29**(13), 1603483 (2017)

[5] COYLE, S., MAJIDI, C., LEDUC, P., and HSIA, K. J. Bio-inspired soft robotics: material selection, actuation, and design. *Extreme Mechanics Letters*, **22**, 51–59 (2018)

[6] WHITESIDES, G. M. Soft robotics. *Angewandte Chemie*, **57**(16), 4258–4273 (2018)

[7] ZHAO, H., O'BRIEN, K., LI, S., and SHEPHERD, R. F. Optoelectronically innervated soft prosthetic hand via stretchable optical waveguides. *Science Robotics*, **1**(1), eaai7529 (2016)

[8] MAJIDI, C. Soft robotics: a perspective — current trends and prospects for the future. *Soft Robotics*, **1**(1), 5–11 (2014)

[9] BHAGAT, S., BANERJEE, H., TSE, Z., and REN, H. L. Deep reinforcement learning for soft, flexible robots: brief review with impending challenges. *Robotics*, **8**(1), 4 (2019)

[10] AKIN, H. L., ITO, N., JACOFF, A., KLEINER, A., PELLENZ, J., and VISSER, A. J. A. M. Robocup rescue robot and simulation leagues. *AI Magazine*, **34**(1), 78 (2013)

[11] CHEN, F., LIU, K., WANG, Y., ZOU, J., GU, G., and ZHU, X. Automatic design of soft dielectric elastomer actuators with optimal spatial electric fields. *IEEE Transactions on Robotics*, **35**(5), 1150–1165 (2019)

[12] HAGHIASHTIANI, G., HABTOUR, E., PARK, S. H., GARDEA, F., and MCALPINE, M. C. 3D printed electrically-driven soft actuators. *Extreme Mechanics Letters*, **21**, 1–8 (2018)

[13] DIAHAM, S., ZELMAT, S., LOCATELLI, M. L., DINCULESCU, S., DECUP, M., LEBEY, T. J. I. T. O. D., and INSULATION, E. Dielectric breakdown of polyimide films: area, thickness and temperature dependence. *IEEE Transactions on Dielectrics and Electrical Insulation*, **17**(1), 18–27 (2010)

[14] LENDLEIN, A. Fabrication of reprogrammable shape-memory polymer actuators for robotics. *Science Robotics*, **3**(18), eaat9090 (2018)

[15] WESTBROOK, K. K., MATHER, P. T., PARAKH, V., DUNN, M. L., GE, Q., LEE, B. M., and QI, H. J. Two-way reversible shape memory effects in a free-standing polymer composite. *Smart Materials and Structures*, **20**(6), 065010 (2011)

[16] MENG, H. and LI, G. A review of stimuli-responsive shape memory polymer composites. *Polymer*, **54**(9), 2199–2221 (2013)

[17] YANG, H., LEOW, W. R., WANG, T., WANG, J., YU, J., HE, K., QI, D., WAN, C., and CHEN, X. 3D printed photoresponsive devices based on shape memory composites. *Advanced Materials*, **29**(33), 1701627 (2017)

[18] MARTINEZ, R. V., FISH, C. R., CHEN, X., and WHITESIDES, G. M. Elastomeric origami: programmable paper-elastomer composites as pneumatic actuators. *Advanced Functional Materials*, **22**(7), 1376–1384 (2012)

[19] GORISSEN, B., CHISHIRO, T., SHIMOMURA, S., REYNAERTS, D., DE VOLDER, M., and KONISHI, S. Flexible pneumatic twisting actuators and their application to tilting micromirrors. *Sensors and Actuators A: Physical*, **216**, 426–431 (2014)

[20] MORIN, S. A., KWOK, S. W., LESSING, J., TING, J., SHEPHERD, R. F., STOKES, A. A., and WHITESIDES, G. M. Elastomeric tiles for the fabrication of inflatable structures. *Advanced Functional Materials*, **24**(35), 5541–5549 (2014)

[21] MOSADEGH, B., POLYGERINOS, P., KEPLINGER, C., WENNSTEDT, S., SHEPHERD, R. F., GUPTA, U., SHIM, J., BERTOLDI, K., WALSH, C. J., and WHITESIDES, G. M. Pneumatic networks for soft robotics that actuate rapidly. *Advanced Functional Materials*, **24**(15), 2163–2170 (2014)

[22] ROCHE, E. T., WOHLFARTH, R., OVERVELDE, J. T., VASILYEV, N. V., PIGULA, F. A., MOONEY, D. J., BERTOLDI, K., and WALSH, C. J. A bioinspired soft actuated material. *Advanced Materials*, **26**(8), 1200–1206 (2014)

[23] YUK, H., LIN, S., MA, C., TAKAFFOLI, M., FANG, N. X., and ZHAO, X. Hydraulic hydrogel actuators and robots optically and sonically camouflaged in water. *Nature Communications*, **8**(1), 14230 (2017)

[24] CONNOLLY, F., POLYGERINOS, P., WALSH, C. J., and BERTOLDI, K. Mechanical programming of soft actuators by varying fiber angle. *Soft Robotics*, **2**(1), 26–32 (2015)

[25] CONNOLLY, F., WALSH, C. J., and BERTOLDI, K. Automatic design of fiber-reinforced soft actuators for trajectory matching. *Proceedings of the National Academy of Sciences of the United States of America*, **114**(1), 51–56 (2017)

[26] KIM, S. Y., BAINES, R., BOOTH, J., VASIOS, N., BERTOLDI, K., and KRAMER-BOTTIGLIO, R. Reconfigurable soft body trajectories using unidirectionally stretchable composite laminae. *Nature Communications*, **10**(1), 3464 (2019)

[27] THRASHER, C. J., SCHWARTZ, J. J., and BOYDSTON, A. J. Modular elastomer photoresins for digital light processing additive manufacturing. *ACS Applied Materials & Interfaces*, **9**(45), 39708–39716 (2017)

[28] WALLIN, T. J., PIKUL, J. H., BODKHE, S., PEELE, B. N., MAC MURRAY, B. C., THERRIAULT, D., MCENERNEY, B. W., DILLON, R. P., GIANNELIS, E. P., and SHEPHERD, R. F. Click chemistry stereolithography for soft robots that self-heal. *Journal of Materials Chemistry B*, **5**(31), 6249–6255 (2017)

[29] WEHNER, M., TRUBY, R. L., FITZGERALD, D. J., MOSADEGH, B., WHITESIDES, G. M., LEWIS, J. A., and WOOD, R. J. An integrated design and fabrication strategy for entirely soft, autonomous robots. *nature*, **536**(7617), 451–455 (2016)

[30] SCHAFFNER, M., FABER, J. A., PIANEGONDA, L., RUHS, P. A., COULTER, F., and STUDART, A. R. 3D printing of robotic soft actuators with programmable bioinspired architectures. *Nature Communications*, **9**(1), 878 (2018)

[31] TRUBY, R. L., WEHNER, M., GROSSKOPF, A. K., VOGT, D. M., UZEL, S. G. M., WOOD, R. J., and LEWIS, J. A. Soft somatosensitive actuators via embedded 3D printing. *Advanced Materials*, **30**(15), 1706383 (2018)

[32] PATEL, D. K., SAKHAEI, A. H., LAYANI, M., ZHANG, B., GE, Q., and MAGDASSI, S. Highly stretchable and UV curable elastomers for digital light processing based 3D printing. *Advanced Materials*, **29**(15), 1606000 (2017)

[33] GE, L., DONG, L., WANG, D., GE, Q., and GU, G. A digital light processing 3D printer for fast and high-precision fabrication of soft pneumatic actuators. *Sensors and Actuators A: Physical*, **273**, 285–292 (2018)

[34] ZHANG, Y. F., NG, C. J. X., CHEN, Z., ZHANG, W., PANJWANI, S., KOWSARI, K., YANG, H. Y., and GE, Q. Miniature pneumatic actuators for soft robots by high-resolution multimaterial 3D printing. *Advanced Materials Technologies*, **4**(10), 1900427 (2019)

[35] STEYRER, B., BUSETTI, B., GYRGY, H., LISKA, R., and STAMPFL, J. Hot lithography vs. room temperature DLP 3D-printing of a dimethacrylate. *Additive Manufacturing*, **21**, 209–214 (2018)

[36] DICKEY, M. D., CHIECHI, R. C., LARSEN, R. J., WEISS, E. A., WEITZ, D. A., and WHITESIDES, G. M. Eutectic gallium-indium (egain): a liquid metal alloy for the formation of stable structures in microchannels at room temperature. *Advanced Functional Materials*, **18**(7), 1097–1104 (2008)

[37] ZHANG, Q., ROACH, D. J., GENG, L., CHEN, H., QI, H. J., and FANG, D. Highly stretchable and conductive fibers enabled by liquid metal dip-coating. *Smart Materials and Structures*, **27**(3), 035019 (2018)

[38] JONES, R. M. *Mechanics of Composite Materials*, 2nd ed., CRC Press, Philadelphia, 71–81 (1998)

Appendix A Mechanics behavior of twisting actuators

To describe the mechanical behavior of the twisting actuators when applying pressure, we consider the stiff fibers and a soft matrix as a fiber-reinforced circular cylindrical shell. Therefore, the twisting angle (θ) is determined by a combination of geometrical parameters of the shell (thickness t, diameter D, and length L), stiffness of fibers (volume fraction $V_{\rm fiber}$ and Young's modulus $E_{\rm fiber}$) and matrix ($V_{\rm matrix}$, $E_{\rm matrix}$), and the applied pressure (P). For simplification, we denote the coordinate system located in the natural directions of the shell as O-xyz while the coordinate system located in the material directions of the fibers as O-123 (see Fig. A1). At this point, we recall from elementary mechanics of materials the transformation equations for expressing stresses in the O-xyz coordinate system in terms of stresses in the O-123 coordinate system[38],

$$\begin{pmatrix} \sigma_x \\ \sigma_y \\ \tau_{xy} \end{pmatrix} = \begin{pmatrix} \cos^2\alpha & \sin^2\alpha & -2\sin\alpha\cos\alpha \\ \sin^2\alpha & \cos^2\alpha & 2\sin\alpha\cos\alpha \\ \sin\alpha\cos\alpha & -\sin\alpha\cos\alpha & \cos^2\alpha-\sin^2\alpha \end{pmatrix} \begin{pmatrix} \sigma_1 \\ \sigma_2 \\ \tau_{12} \end{pmatrix}, \tag{A1}$$

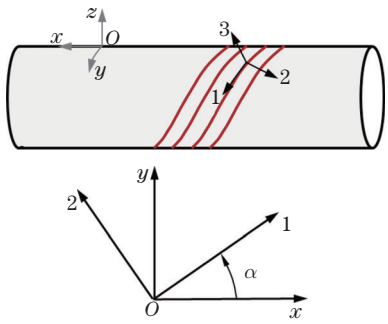

Fig. A1 Schematic of the helically wrapped fiber-reinforced circular cylindrical shell and the rotation of principal material from x-y axes (color online)

where α is the angle from the x-axis to the 1-axis. Here, α is also the lead angle of the helical fibers wrapped around the shell corresponding to the case of a twisting actuator in the main text. Similarly, strains in the O-xyz coordinate system in terms of strains in the O-123 coordinate system can also be expressed as

$$\begin{pmatrix} \varepsilon_x \\ \varepsilon_y \\ \frac{\gamma_{xy}}{2} \end{pmatrix} = \begin{pmatrix} \cos^2\alpha & \sin^2\alpha & -2\sin\alpha\cos\alpha \\ \sin^2\alpha & \cos^2\alpha & 2\sin\alpha\cos\alpha \\ \sin\alpha\cos\alpha & -\sin\alpha\cos\alpha & \cos^2\alpha-\sin^2\alpha \end{pmatrix} \begin{pmatrix} \varepsilon_1 \\ \varepsilon_2 \\ \frac{\gamma_{12}}{2} \end{pmatrix}. \tag{A2}$$

Next, from the constitutive matrix stiffness of the shell, we can express the stress-strain relations in principal material coordinates (O-123) as

$$\begin{pmatrix} \varepsilon_1 \\ \varepsilon_2 \\ \gamma_{12} \end{pmatrix} = \begin{pmatrix} S_{11} & S_{12} & 0 \\ S_{12} & S_{22} & 0 \\ 0 & 0 & S_{66} \end{pmatrix} \begin{pmatrix} \sigma_1 \\ \sigma_2 \\ \tau_{12} \end{pmatrix}, \tag{A3}$$

where the compliances in terms of the engineering constants are $S_{11} = \frac{1}{E_1}$, $S_{22} = \frac{1}{E_2}$, $S_{12} = -\frac{v_{12}}{E_1} = -\frac{v_{21}}{E_2}$, and $S_{66} = \frac{1}{G_{12}}$, respectively. From Eqs. (A1)–(A3), we can obtain the stress-strain relations in natural coordinates of the shell (O-xyz) as

$$\begin{pmatrix} \varepsilon_x \\ \varepsilon_y \\ \gamma_{xy} \end{pmatrix} = \begin{pmatrix} \overline{S}_{11} & \overline{S}_{12} & \overline{S}_{16} \\ \overline{S}_{12} & \overline{S}_{22} & \overline{S}_{26} \\ \overline{S}_{16} & \overline{S}_{26} & \overline{S}_{66} \end{pmatrix} \begin{pmatrix} \sigma_x \\ \sigma_y \\ \tau_{xy} \end{pmatrix}, \tag{A4}$$

where the equivalent compliance constants in the matrix in Eq. (A4) can be expressed as a combination of compliances and lead angle. For a cylindrical shell under internal pressure P, it is not hard to derive the stress components in natural coordinates of the shell as $\sigma_x = \frac{PD}{4t}$, $\sigma_y = \frac{PD}{2t}$, and $\tau_{xy} = 0$. Inserting them into Eq. (A4) gives us the shear strain component as

$$\gamma_{xy} = \overline{S}_{16}\sigma_x + \overline{S}_{26}\sigma_y. \tag{A5a}$$

Namely,

$$\gamma_{xy} = \frac{PD}{4t}\left(\overline{S}_{16} + 2\overline{S}_{26}\right), \tag{A5b}$$

where $\overline{S}_{16} = \left(\frac{2}{E_1} + \frac{2v_{12}}{E_1} - \frac{1}{G_{12}}\right)\sin\alpha\cos^3\alpha - \left(\frac{2}{E_2} + \frac{2v_{12}}{E_1} - \frac{1}{G_{12}}\right)\sin^3\alpha\cos\alpha$, and $\overline{S}_{26} = \left(\frac{2}{E_1} + \frac{2v_{12}}{E_1} - \frac{1}{G_{12}}\right)\sin^3\alpha\cos\alpha - \left(\frac{2}{E_2} + \frac{2v_{12}}{E_1} - \frac{1}{G_{12}}\right)\sin\alpha\cos^3\alpha$, respectively. To obtain the twisting angle θ, a simple displacement-strain relation $\theta = \frac{2\gamma_{xy}L}{D}$ can be adopted. Inserting $\theta = \frac{2\gamma_{xy}L}{D}$ into Eq. (A5b), we hence obtain the following equation for θ:

$$\theta = \frac{PL}{2t}\left(\overline{S}_{16} + 2\overline{S}_{26}\right). \tag{A6}$$

The unknowns E_1, E_2, G_{12}, and υ_{12} in Eq. (A6) can be obtained through E_{fiber}, V_{fiber}, υ_{fiber}, E_{matrix}, V_{matrix}, and υ_{matrix} based on Halpin-Tsai equations, namely,

$$E_1 = E_{\text{fiber}}V_{\text{fiber}} + E_{\text{matrix}}V_{\text{matrix}}, \quad \upsilon_{12} = \upsilon_{\text{fiber}}V_{\text{fiber}} + \upsilon_{\text{matrix}}V_{\text{matrix}}, \tag{A7}$$

$$\frac{E_2}{E_{\text{matrix}}} = \frac{1+\xi_{E_2}\eta_{E_2}V_{\text{fiber}}}{1-\eta_{E_2}V_{\text{fiber}}}, \quad \frac{G_{12}}{G_{\text{matrix}}} = \frac{1+\xi_{G_{12}}\eta_{G_{12}}V_{\text{fiber}}}{1-\eta_{G_{12}}V_{\text{fiber}}}, \tag{A8}$$

$$\eta_{E_2} = \frac{E_{\text{fiber}}/E_{\text{matrix}}-1}{E_{\text{fiber}}/E_{\text{matrix}}+\xi_{E_2}}, \quad \eta_{G_{12}} = \frac{G_{\text{fiber}}/G_{\text{matrix}}-1}{G_{\text{fiber}}/G_{\text{matrix}}+\xi_{G_{12}}}, \tag{A9}$$

where ξ_{E_2} and $\xi_{G_{12}}$ are measures of fiber reinforcement of the composite material that depends on the fiber geometry, packing geometry, and loading conditions. In our case, the cross-section of the fibers in the twisting actuators is almost a square (side length a), thus ξ_{E_2} and $\xi_{G_{12}}$ can be set as 2 and 1, respectively. From the geometry relationship, we have

$$V_{\text{fiber}} = \frac{4a^2L/\sin\alpha}{\pi\left(D^2-(D-2t)^2\right)/4}, \quad V_{\text{matrix}} = 1 - V_{\text{fiber}}. \tag{A10}$$

By solving Eqs. (A6)–(A10), the twisting angle as a function of lead angle α and pressure P can be obtained.

Appendix B Determination of material model for actuator material

In order to accurately capture the mechanical behavior of the actuators, a material model which can account for the features of large deformation needs to be adopted. Here, without losing generality, we consider the material incompressible and use a double-parameter Mooney-Rivlin hyperelastic model. The material parameters are determined through the stress-stretch curve extracted from the tensile tests on no less than five samples (see Fig. B1). In terms of principal stretches, the strain energy density function for the incompressible Mooney-Rivlin material is

$$W = C_1\left(\lambda_1^2+\lambda_2^2+\lambda_3^2-3\right) + C_2\left(\lambda_1^2\lambda_2^2+\lambda_2^2\lambda_3^2+\lambda_3^2\lambda_1^2-3\right), \quad \lambda_1\lambda_2\lambda_3 = 1, \tag{B1}$$

where W, λ_i, and C_i are the strain energy density function, principal stretches, and material-specific parameters, respectively. Then the expressions for the Cauchy stress differences become

$$\sigma_{11} - \sigma_{33} = 2C_1\left(\lambda_1^2-\lambda_3^2\right) - 2C_2\left(\frac{1}{\lambda_1^2}-\frac{1}{\lambda_3^2}\right). \tag{B2}$$

In the case of simple tension, $\sigma_{33} = 0$ and $\lambda_2 = \lambda_3 = 1/\sqrt{\lambda}$. Then we can write

$$\sigma_{11} = \left(2C_1 + \frac{2C_2}{\lambda}\right)\left(\lambda^2 - \frac{1}{\lambda}\right). \tag{B3}$$

Figure B1 presents the best fitting model curve of Eq. (B3) with the parameter values $C_1 = 0.068\ 3\ \text{J}\cdot\text{m}^{-3}$ and $C_2 = 0.032\ 4\ \text{J}\cdot\text{m}^{-3}$.

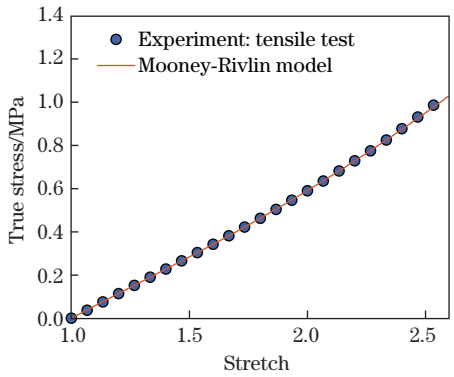

Fig. B1 Mooney-Rivlin constitutive model stress-strain curve against the corresponding experimental data for the material M-2 (color online)